DE GRUYTER Journal of the Mechanical Behavior of Materials 2025; 34: 20250065

Research Article

Sy-Quan Tu*, Huy-Cuong Nguyen and Dang-Quang Ngo

Effect of partially replacing crushed oyster shell as fine aggregate on the shear behavior of short RC beams using GFRP rebar strengthened with TRC: Experimental and numerical studies

https://doi.org/10.1515/jmbm-2025-0065
received December 05, 2024; accepted April 29, 2025

Abstract: An experimental campaign was carried out in order to evaluate the shear behavior of beams. The crushed oyster shell (COS) was replaced partially with natural sand in different mixtures. All specimens maintained the same GFRP rebar arrangement and geometric properties, with several beams strengthened by U-shaped textile-reinforced concrete (TRC) configurations using either two or three layers of carbon textile. Through the three-point bending test on short-span beams, many characteristics reflecting shear performance were evaluated. Beams with TRC strengthening demonstrated enhanced shear resistance, up by 39–44% and by 49–58% in shear capacity observed in specimens, respectively, with two and three textile layers. However, the results also showed a significant reduction in shear performance by an increase to 40% as the replacement ratio of COSs. Additionally, a constitutive finite element model was developed and validated against experimental results, including load–strain relationship and failure mechanism. The simulation accurately predicted the load–deflection behavior with less than 10% deviation from the experimental data and effectively captured failure patterns. The work reported in this study indicates a luminous trend application of oyster shell concrete and gives a reference for improving the mechanical properties of beams strengthened by TRC.

Keywords: oyster shell concrete, shear performance, textile-reinforced concrete, glass fiber-reinforced polymer, numerical simulation, fine-grained concrete

Nomenclature

AQS	auto quantitative spectrum
COS	crushed oyster shell
GFRP	glass fiber-reinforced polymer
LVDT	linear variable differential transformer
OSC	oyster shell concrete
TRC	textile-reinforced concrete
XRD	X-ray diffraction
$\bar{\sigma}_{\max}$	maximal principal effective stress
σ_{b0}/σ_{c0}	biaxial stress ratio
E_0	initial elastic stiffness of concrete
G_{ch}	crushing energy per unit area
G_f	fracture energy per unit area
K_c	ratio of second stress invariant on the tensile meridian to compressive meridian at the initial yield
d_c	compressive damage parameter
d_t	tensile damage parameter
f_c'	compressive strength of concrete (g_r = 0.012 to 0.021, g_t = 0.0069)
f_r	modulus of rupture
f_t	direct tensile strength
$\bar{p}$	Von Mises-equivalent effective stress
$\bar{q}$	hydrostatic pressure
w_c	unit weight of concrete
ε_{c0}	compressive strain at peak
ε_c^{in}	inelastic compression strain
ε_c^{pl}	plastic strain under compression
ε_{oc}^{el}	compressive elastic strain
ε_{ot}^{el}	tensile elastic strain
ε^{pl}	equivalent plastic strain
ε_{t0}	tensile strain at peak
ε_t^{ck}	tensile cracking strain
ε_t^{pl}	plastic strain under tension
σ_{b0}	initial equibiaxial compressive yield stress
σ_{c0}	initial uniaxial compressive yield stress

*** Corresponding author: Sy-Quan Tu,** Faculty of Construction Engineering, University of Transport and Communications, Hanoi, Vietnam, e-mail: tusyquan@utc.edu.vn
Huy-Cuong Nguyen, Dang-Quang Ngo: Faculty of Construction Engineering, University of Transport and Communications, Hanoi, Vietnam

μ	ductility index
F	yield surface function
Δu	mid-span deflection at ultimate load
Δy	mid-span deflection at the yield limit
ϵ	eccentricity parameter
ρ	mass density
σ_{t0}	uniaxial tensile stress at failure
υ	Poisson's ratio
Φ	plastic potential function
Ψ	dilatation angle
λ	viscosity parameter

1 Introduction

The reuse of oyster shells as a component of concrete is a classic idea. The first structures built with this kind of concrete were notified in North America in the sixteenth century by Spanish explorers. During that period, limestone, a key material for making construction lime, was not accessible to the early settlers. As a result, slaked lime had to be imported or produced by calcining oyster shells, which were abundant along the coasts of what is now Georgia, Florida, and South Carolina [1]. The process involved burning oyster shells to create slaked lime, which was then combined with water, sand, ash, and seashell fragments to produce a type of concrete known as Tabby (Tabby concrete) [2]. Later, due to the appearance of cement concrete, outstanding in terms of strength and durability, this kind of material gradually disappeared and was forgotten for a long time [1]. Nowadays, the demand for urban construction is rising, leading to overexploitation of aggregate, causing resource depletion, and negatively affecting the ecological environment. Hence, the finding of the new friendly aggregate types is a noticeable trend. In this context, Steven *et al.* [3] conducted a comparison of four material structures, including bone, deep sponge, seashell, and cement concrete, at different scales: macro, meso, micro, and nano scales. The research results concluded that, at the mesoscale, seashells are constituted from several layers of Aragonite leaves, a type of mineral belonging to the group calcium carbonate ($CaCO_3$). Research conducted by Monita *et al.* [4] demonstrated that substituting traditional aggregates with seashells notably enhances the tensile and flexural strength of concrete. However, the compressive strength and modulus of elasticity were found to vary depending on the size of the aggregates used. The aggregate size also dramatically affects the permeability and ability of an object to absorb and release water retention, according to a review by Uchechi *et al.* [5]. However, the chloride ions in unwashed oyster shells would induce accelerated corrosion effects on the internal steel rebar [6]. Therefore, non-metallic reinforcement such as fiber-reinforced polymer (FRP) rebar or carbon textile with many advantages over steel rebar, such as lower density, higher tensile strength, electrical and magnetic insulator, and excellent corrosion resistance [7–10], could be more suitable for promoting serviceability also durability of structure members [11–19]. Oyster shell concrete (OSC) has been recognized for its environmental benefits. However, it typically exhibits lower mechanical strength compared to conventional concrete of the same grade. This reduction in strength, particularly in terms of compressive and shear performance, necessitates strengthening solutions to enhance its structural integrity. Despite the increasing interest in sustainable construction materials, publications addressing the strengthening of OSC remain limited. Among the research on the shear performance of GFRP bar-reinforced seawater sea-sand concrete beams [20–22], Xing *et al.* [20] concluded that the existence of certain content of seashell governed the decrease of the stiffness, cracking load, and ultimate shear strength of considered beams. From several studies, the use of U-shaped configurations by TRC or FRP materials often provides high strengthening efficiency for RC beams. [23–25]. Due to poor compatibility with the concrete surface and high dependency on moisture and temperature conditions, the use of epoxy as a bonding agent in FRP strengthening is inappropriate in certain cases. Additionally, cracks that develop on the concrete substrate are usually concealed by FRP material, making maintenance work more challenging [26].

In recent years, textile-reinforced concrete (TRC) has been applied through various test programs and *in situ* projects for infrastructure development, such as bridge construction and building or tunnel domains, as summarized by Tran and Tu [27]. Textiles are made by knitting yarns (or rovings), with each roving consisting of thousands of filaments. The filament, which is the main load-bearing component in the textile grid of TRC, consists of 400–7,000 individual yarns with diameters ranging from 5 to 30 µm. Depending on the structure of each type of textile grid, the packing density of these fibers varies, as in the study of Brameshuber [10]. Experiments conducted by Peled *et al.* [28,29] also indicated that the bonds between the filament and cement matrix depend on the geometry characteristic of the textile grid, manufacturing technology, and the material and dimension of the textile mesh. TRC is truly an innovative composite material known for its superior tensile strength and durability, making it an ideal solution for structural strengthening or new smart structures. The contribution of TRC improves the load-carrying capacity of structural integrity. Compared to fewer strengthening layers, the greater strengthening layers of TRC provide a higher stiffness and more effective shear resistance to RC beams by allowing them to restrain the growth of diagonal cracks [26]. Several studies have investigated the shear behavior of TRC-strengthened beams, including works by Si Larbi *et al.*, Tran *et al.*, and Rossi *et al.* [30–32], and the use of innovative materials like TRC to enhance the shear capacity of reinforced concrete beams is gaining increasing attention [33,34]. However, these studies have primarily focused on strengthening conventional concrete beams, leaving a gap in research concerning the application of TRC for alternative materials, such as OSC. In light of this, TRC has emerged as a promising strengthening technique for improving the load-bearing capacity of OSC. TRC offers several advantages, including increased tensile strength, crack resistance, and the ability to transform failure modes from brittle to more ductile behavior. It is necessary to clarify the effects of TRC composites in improving the mechanical properties of continuous RC beams through experimental and analytical methods. This research aims to fill the gap by investigating the shear behavior of short-span beams reinforced with GFRP bars and strengthened with TRC, specifically focusing on beams made from OSC. The study also examines how varying the number of TRC layers and the proportion of crushed oyster shells (COSs) in the concrete mix impacts the overall shear performance. Through this work, the research contributes valuable insights into enhancing the mechanical properties of OSC, promoting its application in sustainable construction.

2 Experimental approach

2.1 Test specimens

In this research, nine concrete beams were fabricated to examine the shear performance of beams that were reinforced with GFRP bars and enhanced with carbon TRC. The beams were divided into three groups according to the proportion of COSs that partially replaced river sand in the concrete mix: 0, 20, and 40%. For each concrete mix, three beams were cast. Table 1 describes the level of COS replacement and the strengthening applied to each beam.

The first beam in each group served as a control specimen and was not strengthened with TRC. The second and third beams were upgraded with two and three carbon textile layers. All beams were constructed with uniform dimensions, measuring 150 mm in width, 250 mm in height, and 900 mm in length. The span for the three-point bending tests was established at 600 mm to create a shear-critical region and accurately assess the shear performance of the beams.

Longitudinal reinforcement in each beam was provided using GFRP bars, with three Ø16 bars placed in the bottom layer and two Ø16 bars in the top layer (Figure 1). Transverse reinforcement was provided by Ø6 GFRP stirrups, positioned at 100 mm intervals along the beam's length. This uniform reinforcement layout ensured that the only variables influencing the results were the proportion of COSs and the presence or absence of TRC strengthening. Two TRC configurations were tested: one with two layers and another with three layers of carbon textiles, applied to the two side faces and the bottom face of the beams. This setup was designed to assess the impact of textile layering on shear performance, especially in beams where COSs partially replaced natural sand. The TRC system was intended to offset any potential strength reductions from the use of alternative aggregates, thereby enhancing the overall shear resistance of the beams.

2.2 Identification of materials

2.2.1 OSC

The oyster shells dedicated to this study are Pacific Oyster. The aggregates, including natural sand, COSs, and 5 mm ×

Table 1: Description of specimens classified by crushed OSC and the strengthening method

Group	Specimen	Description
G1: 0% COS	TCB-R	Control beam
	TCB-2T90	Beam with 0% COS, strengthened with two carbon layers
	TCB-3T90	Beam with 0% COS, strengthened with three carbon layers
G2: 20% COS	20OSB-R	Control beam, using 20% COS
	20OSB-2T90	Beam with 20% COS, strengthened with two carbon layers
	20OSB-3T90	Beam with 20% COS, strengthened with three carbon layers
G3: 40% COS	40OSB-R	Control beam, using 40% COS
	40OSB-2T90	Beam with 40% COS, strengthened with two carbon layers
	40OSB-3T90	Beam with 40% COS, strengthened with three carbon layers

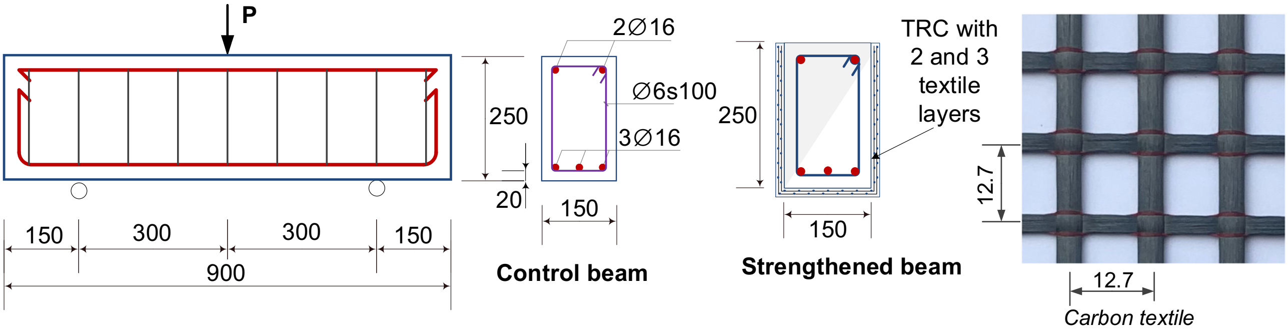

Figure 1: Details of test beams.

10 mm gravel, are washed and dried before concrete pouring. The primary source of fine aggregates is natural sand extracted from the Song Da River, with a fineness modulus (Mk) of 2.5 and a density of 2.67 g/cm^3. Besides, the oyster shells are crushed so that the largest particles pass through a 4.75 mm sieve, as illustrated in Figure 2. The coarse aggregate, 5 mm × 10 mm gravel, was selected with a maximum grain size smaller than 12.5 mm. The grain composition of both fine and coarse aggregates meets the ASTM C33 [35] recommendations and is shown in Figure 3.

In this case, the chemical composition of oyster shells was analyzed using the Auto Quantitative Spectrum (AQS) method using an X-ray diffraction (XRD) spectrometer, and the experimental results are presented in Figure 4. Concretely, the percentage of $CaCO_3$ content is mainstream, accounting for 73.34%. Meanwhile, other compounds such as Richterite $Na_2CaMg_5(Si_8O_{22})(OH)_2$ and Leucite low KAlSi2O6 occupy around 5.73 and 4.07%, respectively. The loss in calcination content of oyster shells is estimated to be less than 16.86%. This analysis confirms the optimal replacement for fine aggregate by a COS in the scope of sustainable development.

In this study, the fine aggregate component was partially substituted with COSs at replacement levels of 0, 20, and 40%. In contrast, other materials, such as cement, fly ash, and coarse aggregate, remained constant. Due to the higher water absorption capacity of oyster shells compared to natural sand, the water content added to the mixtures containing partial replacement of oyster shells is greater than that of the control mixtures.

This approach enables the evaluation of the effects of COS inclusion on the mechanical properties of concrete when used as a partial replacement for fine aggregate. Specifically, three concrete mixtures were prepared, each consisting of cement, fine aggregate, coarse aggregate, fly ash, and a superplasticizer admixture, with a water-to-binder ratio of 0.36. The traditional concrete mixture (0% COS) was designed to achieve a target strength of C50, based on ACI 211.4R-08 [36], and further refined through experimental adjustments. C50 is the compressive strength that meets the requirements of typical construction works. The detailed composition of the concrete mixtures is provided in Table 2.

2.2.2 Glass fiber-reinforced polymer (GFRP)

For this experiment, GFRP rebars with a braided surface treatment were selected. The matrix resins consisted of epoxy, while the filaments were made of AR-glass fiber

Figure 2: Extraction of Pacific Oyster shell at different scales. (a) Oyster shells are washed and dried before grinding. (b) Grain sizes from 0.15 to 4.75 mm of COSs.

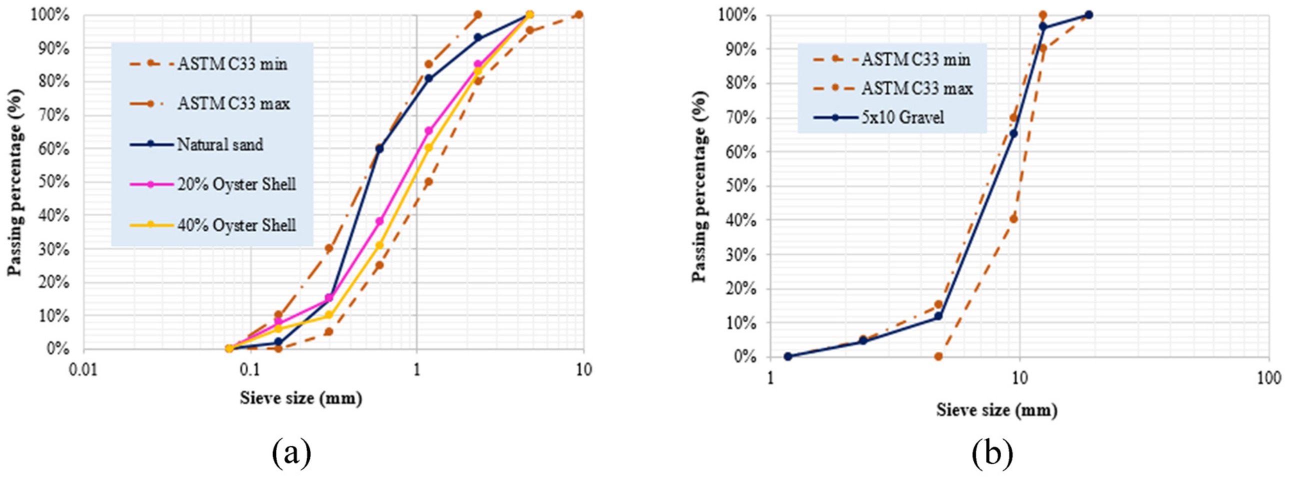

Figure 3: The size distribution curve conforms to the requirement of ASTM C33. (a) Fine aggregate. (b) Coarse aggregate.

reinforcement. Tensile and compressive tests were conducted using a SANS 3000 kN testing machine to assess the material properties of the GFRP, following the ASTM D7205M standard [37]. Due to the relatively low shear and compressive strength of GFRP, both ends of the reinforcing bars were encased in 32 mm-diameter steel pipes coated with Sikadur 731 resin to prevent damage from the testing machine's clamping jaws. The specimens were loaded using displacement control at a rate of 1 mm/min. The experimental results are summarized in Table 3.

2.2.3 TRC

The specimens, measuring 40 mm × 40 mm × 160 mm, were tested in accordance with ASTM C348-21 [38] for flexural

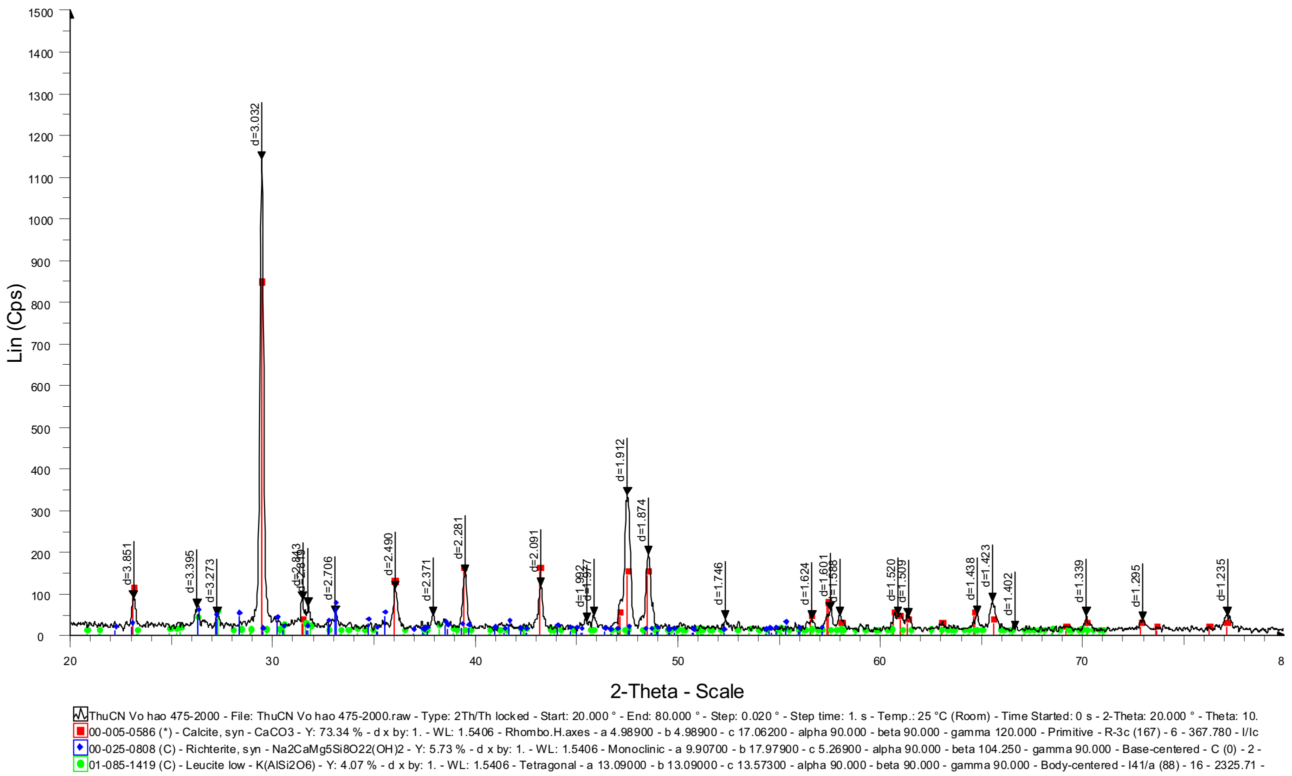

Figure 4: X-ray diffraction spectrum of Pacific Oyster shell specimens.

Table 2: Composition of concrete mixtures per cubic meter

Materials	Units	Traditional concrete	20% OSC	40% OSC
PC40 fine cement	kg	454.5	454.5	454.5
Natural sand dried	kg	635.7	508.5	381.4
5 × 10 gravel dried	kg	1040	1040	1040
COSs dried	kg	0	50.5	101.0
Water	l	208.9	212.6	216.2
Fly ash (F)	kg	80.2	80.2	80.2
Superplasticizer admixture	l	5.6	5.6	5.6

Table 3: Characteristic of GFRP rebars

	Nominal rebar diameters (mm)		
	Ø6	**Ø16**	**Ø20**
Cross-sectional area (mm^2)	19.6	165	240.4
Elastic modulus (MPa)	44961.5 s = 1590.6 Cv = 4%	45253.6 s = 3060.3 Cv = 7%	45843.8 s = 2286.5 Cv = 5%
Tensile strength (MPa)	822.5 s = 20.6 Cv = 3%	812.5 s = 28.7 Cv = 4%	811.3 s = 37.9 Cv = 5%
Compressive strength (MPa)	170.8 s = 15.9 Cv = 9%	178.5 s = 14.9 Cv = 8%	185.8 s = 13.8 Cv = 7%

strength and ASTM C349-18 [39] for compressive strength of hydraulic-cement mortars (utilizing sections of prisms broken in flexure). A total of six specimens were tested to ensure statistical reliability, and the tests were conducted in a controlled environment as specified in the standards. To improve the shear strength of RC beams, a TRC system was employed, consisting of fine-grained concrete with a compressive strength of 48.3 MPa and a flexural tensile strength of 5.7 MPa, paired with carbon fiber textile reinforcement. The concrete mix, featuring a maximum aggregate size of 0.63 mm, was optimized for strong bonding with carbon textiles and included high-performance cement, fly ash, and a superplasticizer to enhance durability. As for the carbon fiber mesh, the mechanical properties are sourced directly from the manufacturer's specifications. The carbon textile reinforcement used was the SITgrid017, which featured an orthogonal grid with 12.7 mm spacing and a surface weight of 578 g/m^2. The textile's reinforcement cross-sectional area measured 151.18 mm^2/m in both directions, comprising 78 rovings per meter, with each roving containing 48,000 fibers. The tensile strength of the textile was 2,890 MPa, while the elastic modulus was 185 GPa. A styrene–butadiene coating was applied to the textiles to improve adhesion with the concrete matrix.

2.3 Fabrication of the specimen procedure

The fabrication of the specimens was conducted with careful precision to ensure uniformity and reliability across all experimental results. All three types of concrete were mixed in a drum mixer until a homogeneous consistency was achieved, after which it was poured into formwork to cast the beams. Prior to pouring the concrete, the GFRP reinforcing cages were assembled outside the formwork and inserted afterward after attaching strain gauges to the respective rebars and stirrups (Figure 5). After casting, the beams were cured in water for 28 days under controlled laboratory conditions.

Upon completing the fabrication process, two beams from each group were wrapped with either two or three layers of carbon textiles. In contrast, the remaining beams were kept unstrengthened as control specimens. The TRC

Figure 5: Fabrication of RC beams with COS aggregates.

Figure 6: Application of TRC strengthening layers on RC beams.

strengthening procedure was performed in accordance with the guidelines outlined in ACI 549.4R-20 [40]. Preparation of the substrate, including the removal of corrosion debris and roughening of the surface, was conducted to ensure optimal bonding between the TRC and concrete substrate. A 5 mm-thick layer of fine-grained concrete was first applied to the beam surfaces using a metal trowel. The carbon textile was then embedded into this layer, ensuring full integration into the concrete matrix. Subsequent layers of fine-grained concrete were applied to completely cover the textile, with this process repeated until the specified number of textile layers was achieved, as illustrated in Figure 6.

2.4 Test setup and measurement

For the three-point bending test arrangement, each beam was placed on two supports, spaced 600 mm apart, with the load applied at the midpoint to induce shear forces in the beam's critical region (Figure 7). The two supports are cylindrical with a diameter of 80 mm, ensuring that the beam can freely rotate at the contact points. The loading frame and load application were controlled by the displacement method, in which the loading rate was maintained at 0.5 mm/min, and the test was conducted until failure. Deflections were recorded using a Linear Variable Differential Transformer (LVDT) positioned at the mid-span of the beam. Additionally, strain gauges were attached to the GFRP rebar and stirrups to monitor the strain distribution during loading. This arrangement allowed for a comprehensive analysis of the load–deflection behavior of the beams, as well as the effectiveness of the TRC strengthening in improving shear capacity.

Simultaneously, several cylindrical concrete specimens measuring 150 mm × 300 mm were cast and cured in water at a controlled temperature of 22°C for 28 days. These specimens were used to assess various mechanical

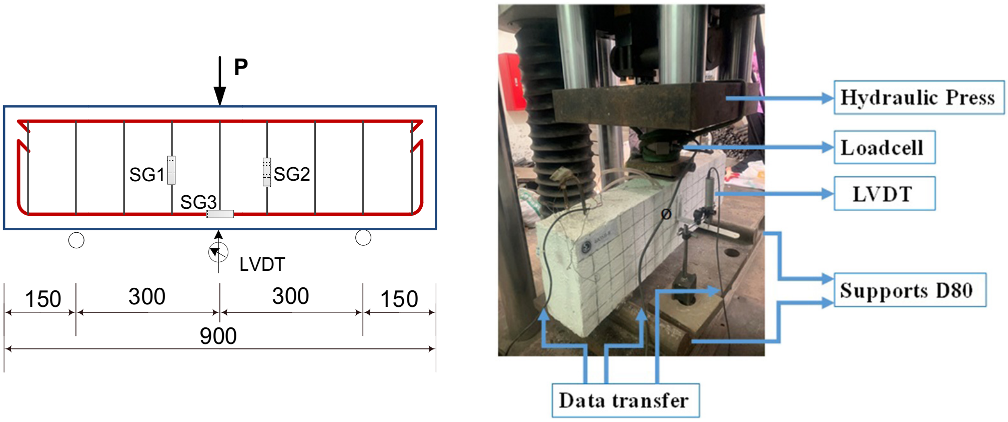

Figure 7: Test setup.

Table 4: Mechanical properties of different concrete mixtures

Category	Units	Concrete mixture			Fine-grained concrete
		Traditional concrete	20% OSC	40% OSC	
Compressive strength	MPa	56.8	45.3	41.2	48.3
		s = 1.83	s = 2.92	s = 3.16	s = 2.92
		Cv = 3%	Cv = 6%	Cv = 8%	Cv = 6%
Flexural tensile strength	MPa	8.6	6.9	5.8	6.2
		s = 0.411	s = 0.445	s = 0.471	s = 0.386
		Cv = 5%	Cv = 6%	Cv = 8%	Cv = 6%
Modulus of elasticity	MPa	33764.3	27555.2	24139.1	28,154
		s = 2192.1	s = 2087.6	s = 944.8	s = 1382.3
		Cv = 6%	Cv = 8%	Cv = 4%	Cv = 5%

properties, including compressive strength and static modulus of elasticity. These tests conform to specifications ASTM C39 [41] and ASTM C469, respectively [42]. Moreover, to assess the flexural tensile strength, four-point bending tests were carried out on rectangular specimens with dimensions of 100 mm × 100 mm × 400 mm. The testing procedure adhered to the ASTM C78 guidelines [43], as outlined in Table 4. The characteristics of different mixtures are summarized in Table 4 and Figure 8.

3 Computational methods

3.1 Finite element analysis and boundary conditions

In this study, nine 3D finite element models were constructed using Abaqus/Explicit [44] to replicate the experimental tests carried out on the specimens, as described in Section 2. The concrete and steel plate domains were discretized using the C3D8R from the Abaqus material library, which is a fully integrated 3D brick element with eight linear nodes. Each element had dimensions of 15 mm × 15 mm × 15 mm. Depending on the type of specimen, the overall quantity of elements varies between 9,600 and 12,960. For the reinforcement, T3D2 truss elements were employed to represent the behavior of the GFRP bars. Against the boundary condition, the models were established respecting the three-point bending principle with the applying force controlled by displacement at the middle and two supporting pins, which could rotate around its symmetrical axis. For the concrete–TRC interface, a tie constraint was applied to model the interaction between the two materials. Compared to the flexural test, the shear test gives a lower deflection at the midspan of beams, leading to the more efficient strengthening of TRC (Figure 9). Thus, the assumption that all materials have a perfect bond to another one is chosen.

3.2 Input parameters for the models

The input parameters for these models were primarily based on those established by Vervloet *et al.* [45]. To model the behavior of concrete, the well-known concrete damage

Figure 8: The perspective of experimental work for determining the mechanical properties of traditional concrete and OSC.

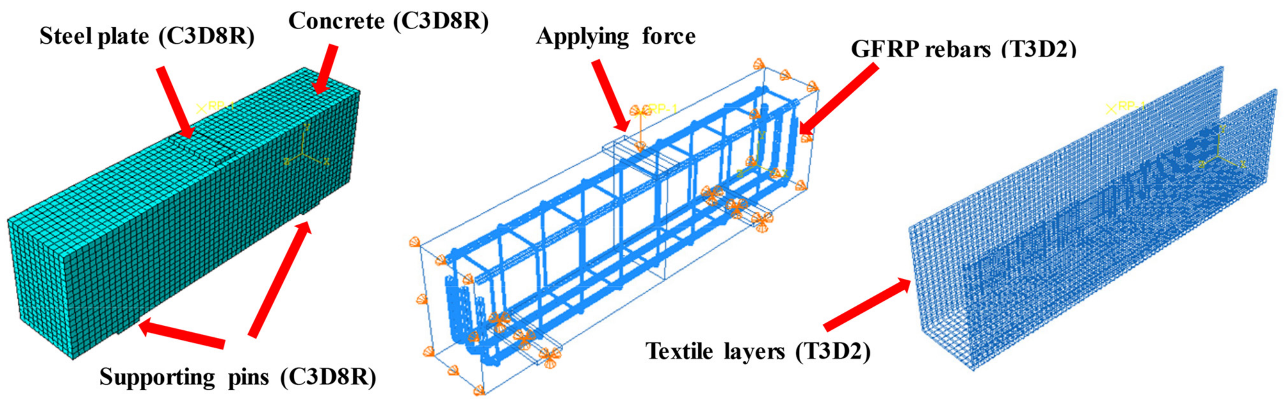

Figure 9: Mesh discretization and boundary conditions for the modeling of RC beam with/without strengthening.

plasticity (CDP) model was utilized. This model, initially introduced by Hognestad [46], has been further developed by various researchers, including Nguyen *et al.*, Lubliner *et al.*, and Lee and Fenves [47–49]. CDP is a non-associated plasticity model, wherein the plastic potential (Φ) is a Drucker–Prager hyperbolic function. This function combines with a distinct function of yield surface (F), according to Ayhan *et al.* [50], which controls the stress–strain relationships, as depicted in Figures 11 and 12:

$$\Phi = \sqrt{(\epsilon\sigma_{t0}\tan\Psi)^2 + \bar{q}^2} - \bar{p}^2\tan\Psi. \quad (1)$$

Here, Ψ is the dilatation angle taken against the deviatoric stress plane; ϵ is the eccentricity parameter; σ_{t0} is the uniaxial tensile stress at failure; $\bar{q}$ is the hydrostatic pressure; and $\bar{p}$ is the von Mises-equivalent effective stress, defined by Eqs. (2) and (3), respectively:

$$\bar{q} = \sqrt{\frac{3}{2}(s:s)}, \quad (2)$$

$$\bar{p} = -\frac{1}{3}tr(\bar{\sigma}). \quad (3)$$

In Eq. (2), s denotes the deviatoric part of the effective stress tensor:

$$F = \frac{1}{1-\alpha}(\bar{q} - 3\alpha\bar{p} + \beta(\varepsilon^{\mathrm{pl}})\langle\bar{\sigma}_{\max}\rangle - \gamma\langle\bar{\sigma}_{\max}\rangle) - \bar{\sigma}_{\mathrm{c}}(\varepsilon_{\mathrm{c}}^{\mathrm{pl}}) = 0. \quad (4)$$

In Eq. (4), $\bar{\sigma}_{\max}$ corresponds to the maximal principal effective stress; $\varepsilon^{\mathrm{pl}}$ is equivalent plastic strain; and α, β, and γ are calculated as follows:

$$\alpha = \frac{(\sigma_{b0}/\sigma_{c0}) - 1}{2(\sigma_{b0}/\sigma_{c0}) - 1}; 0 \le \alpha \le 0.5, \quad (5)$$

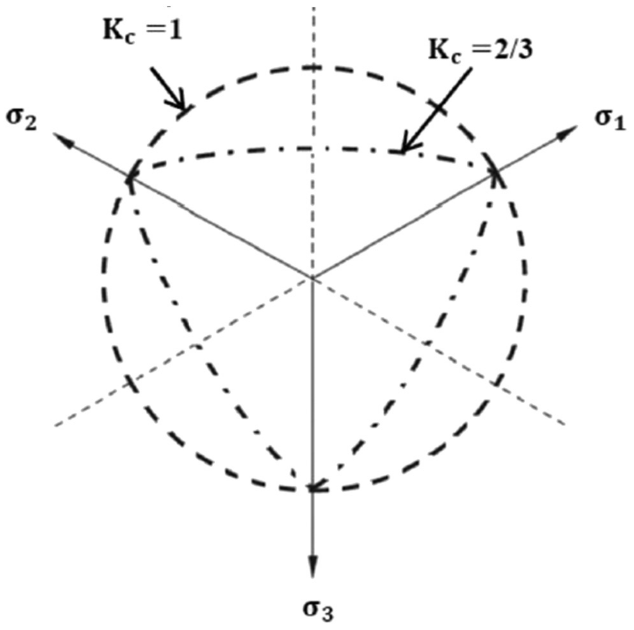

Figure 10: Effect of different K_c values to yield surfaces in the deviatoric plane under the Drucker–Prager yield criterion.

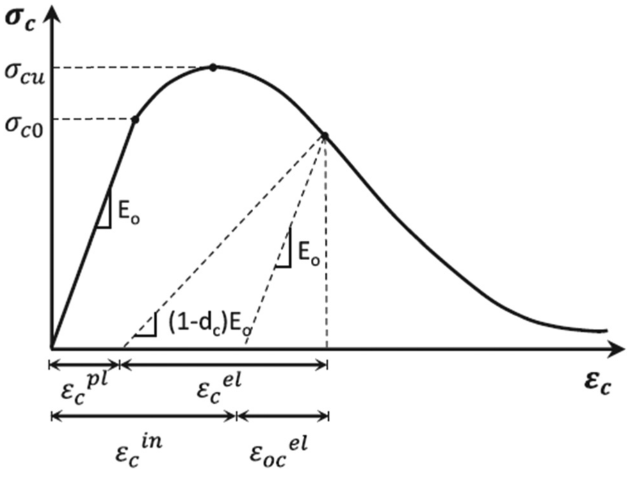

Figure 11: Stress–strain curve and concerning parameters of concrete under uniaxial compression of the CDP model.

$$\beta = \frac{\bar{\sigma}_c(\varepsilon_c^{pl})}{\bar{\sigma}_t(\varepsilon_t^{pl})}(1 - \alpha) - (1 + \alpha), \tag{6}$$

$$\gamma = \frac{3(1 - K_c)}{2K_c - 1}, \tag{7}$$

where σ_{b0} and σ_{c0} are initial equibiaxial compressive yield stress and initial uniaxial compressive yield stress, respectively; and K_c is the ratio of the second stress invariant on the tensile meridian to the compressive meridian at the initial yield.

This ratio affects the shape of the yield surface on the deviatoric plane. Figure 10 illustrates the contribution of the chosen K_c values to evolution of yield surfaces in the deviatoric cross-section (refer to Kazemi *et al.* [51]).

As shown in Figures 11 and 12, inelastic compression strain ε_c^{in} and tensile cracking strain ε_t^{ck} are obtained by employing Eqs. (8) and (9), in which ε_{oc}^{el} and ε_{ot}^{el} refer to the compressive elastic strain and the tensile elastic strain, respectively, determined by Eqs. (10) and (11):

$$\varepsilon_c^{in} = \varepsilon_c - \varepsilon_{oc}^{el}, \tag{8}$$

$$\varepsilon_t^{ck} = \varepsilon_c - \varepsilon_{ot}^{el}, \tag{9}$$

$$\varepsilon_{oc}^{el} = \frac{\sigma_c}{E_o}, \tag{10}$$

$$\varepsilon_{ot}^{el} = \frac{\sigma_t}{E_o}. \tag{11}$$

The elastic stiffness of concrete is usually degraded under applied load compared to the initial stiffness. This diminution is characterized by the tensile and compressive damage parameters, d_t and d_c. According to Tawfik *et al.* [52], these coefficients are as follows:

$$E_c = (1 - d_c)E_o, \tag{12}$$

$$E_t = (1 - d_t)E_o, \tag{13}$$

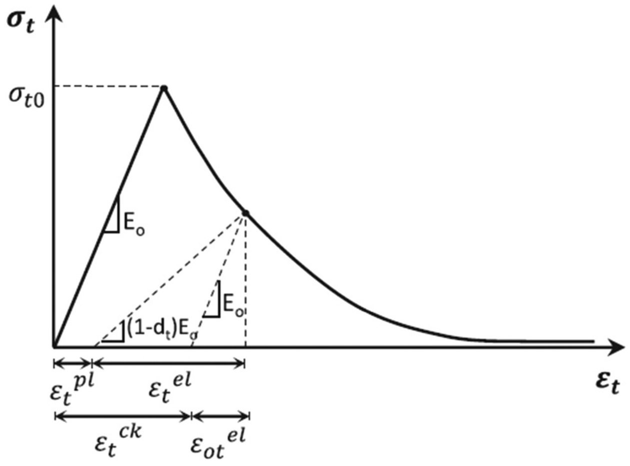

Figure 12: Stress–strain curve and concerning parameters of concrete under uniaxial tension of the CDP model.

$$d_c = 1 - \frac{\sigma_c}{\sigma_{cu}}, \tag{14}$$

$$d_t = 1 - \frac{\sigma_t}{\sigma_{t0}}. \tag{15}$$

The plastic strain under compression or tension can be determined using Eqs. (16) and (17):

$$\varepsilon_c^{pl} = \varepsilon_c^{in} - \frac{d_c}{1 - d_c}\frac{\sigma_c}{E_o}, \tag{16}$$

$$\varepsilon_t^{pl} = \varepsilon_t^{ck} - \frac{d_t}{1 - d_t}\frac{\sigma_t}{E_o}. \tag{17}$$

Especially in Abaqus, the compressive damage parameter d_c (DAMAGEC) and the tensile damage parameter d_t (DAMAGET) under uniaxial loading are also the function of other variables, in which f_{tm} and f_{cm} depend on the tensile or compressive strengths of concrete, G_f and G_{ch} represent fracture and crushing energies per unit area and l_{eq} reflect the geometric element properties of the mesh, like in Antoniou *et al.* [53]:

$$d_t = d(\varepsilon_t^{pl}, f_{tm}, G_f, l_{eq}), \tag{18}$$

$$d_c = d(\varepsilon_c^{pl}, f_{cm}, G_{ch}, l_{eq}). \tag{19}$$

In the current study, the compressive strength and modulus of elasticity values were derived from experimental measurements, while the tensile strength values were calculated from those of flexural tensile strength, following the guidance of ACI224.2R-92 [54]. The modulus of rupture (f_r) and direct tensile strength (f_t) are determined using Eqs. (20) and (21), respectively:

$$f_r = g_r\sqrt{w_c f_c'}, \tag{20}$$

$$f_t = g_t\sqrt{w_c f_c'}, \tag{21}$$

where w_c is the unit weight of concrete (kg/m^3), f_c' is the compressive strength of concrete (MPa), $g_r = 0.012 - 0.021$, and $g_t = 0.0069$.

Therefore, the direct tensile strength can be taken between 33 and 58% of the flexural tensile strength. These values serve to establish the stress–strain diagram proposed by Zheng *et al.* [55], validated for ordinary concrete, as presented in Figure 13. Against this model, the values at the peak of ultimate strengths generating the shape of stress–strain evolution in both ascendant and descendent branches could be defined experimentally, as reported in Table 5. The tensile strain at peak (ε_{t0}) is calculated by employing Eq. (22); meanwhile, the compressive strain at peak (ε_{c0}) is formulated based on the modified Hognestad model for the compressive behavior of concrete (refer to Madandoust *et al.* [56]):

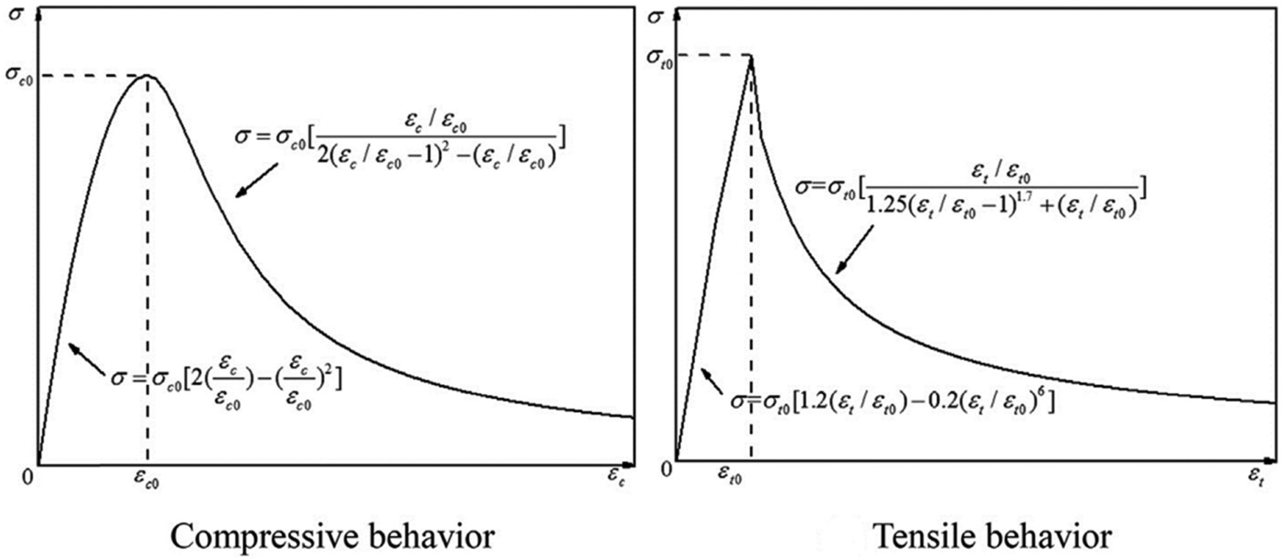

Figure 13: Stress–strain diagram of the CDP constitutive model for concrete.

$$\varepsilon_{t0} = \frac{\sigma_{t0}}{E_0}, \tag{22}$$

$$\varepsilon_{c0} = 1.8\frac{\sigma_{c0}}{E_0}. \tag{23}$$

The overall mechanical properties of other materials used for the model are outlined as follows (Figure 14).

Among the multi-plasticity parameters of the CDP model described by Vervloet *et al.* [45], Tawfik *et al.* [52], and Kazemi *et al.* [51], the first one is the dilatation angle ψ, representing the mechanic behavior of concrete under confined stress. The recommended values range from 30° to 45° (refer to Shawki Ali *et al.* [57]).

The second one is flow potential eccentricity ϵ, reflecting the ratio between the tensile strength and compression strength, and the recommended value is 0.1. The third parameter is the biaxial stress ratio, σ_{b0}/σ_{c0}, which ranges always taken from 1.00 to 1.16. The fourth parameter is the shape factor K_c, and its default values vary from 0.667 to 1.0. The last parameter is viscosity λ, which allows the enhancement of the rate of solution convergence in certain sufficiently small problem steps with chosen values from 0.0001 to 0.008 [57,58]. The Poisson's ratio of concrete is usually taken from 0.15 to 0.25, according to Ahmed [59] or Pal [60], and its value increases when the compressive strength of concrete decreases. The details concerning the mechanical parameters of using materials in the models are displayed in Table 5.

4 Results and discussion

4.1 Bearing mechanism and load–deflection relationship

First, the shear performance of the nine beams was systematically evaluated through three-point bending tests. The results provided valuable insights into the influence of crushed OSC, the effectiveness of TRC strengthening, and the structural behavior of the investigated beams.

During testing, distinct failure modes were observed, with notable differences between the control and TRC-strengthened beams. The control beams (unstrengthened) exhibited a brittle shear failure, characterized by the rapid expansion of diagonal shear cracks, typically initiating near the support and propagating toward the load application point (Figure 15). This led to a sudden and catastrophic failure once the critical shear stress was exceeded. In contrast, the TRC-strengthened beams demonstrated a more ductile failure mode. The TRC layers effectively delayed shear cracking, with beams reinforced with two layers of carbon textiles showing smaller, more distributed cracks. Beams with three TRC layers exhibited even finer crack patterns, indicating a higher degree of crack control and stress redistribution within the beams, thus preventing the sudden shear failures observed in the control specimens.

Table 5: Mechanical parameters of materials used for modeling

Index properties	Elastic modulus E_o (MPa)	Poisson's ratio υ	Tensile strength σ_{t0} (MPa)	Strain at peak ε_{t0} (με)	Compressive strength σ_{c0} (MPa)	Strain at peak ε_{c0} (με)	Mass density ρ (kg/m^3)
Steel	210,000	0.3	578	2752.38	264	1257.14	7,800
Textile	185,000	0.25	2890	15621.62	N/A	N/A	1,500
GFRP stirrup	44,962	0.28	823	18304.35	171	3803.21	2,100
GFRP long. reinforcement	45,253	0.28	813	17965.66	179	3955.54	2,100
Fine-grained concrete	28,154	0.18	2.52	89.51	48.3	3088.02	2,450
Traditional concrete	33,764	0.18	3.01	89.15	56.8	3028.08	2,512
20% OSC	27,555	0.21	2.46	89.28	45.4	2965.70	2,437
40% OSC	24,139	0.21	2.66	110.20	41.3	3079.66	2,364

Adhesive strength between the filament textile and concrete: 24 N/mm

CDP model parameters

$\psi = 36°$; $K_c = 2/3$; $\epsilon = 0{,}1$; $\sigma_{bo}/\sigma_{co} = 1{,}16$; $\lambda = 1E - 4$

Load–deflection curves for each beam group were plotted to analyze the structural behavior under increasing loads. Overall, regarding the load–deflection curves depicted in Figures 16–18, a good agreement exists between the numerical and experimental results. The response of load–deflection of all beams is approximately linear up to the first crack formation. Subsequently, the curves turned non-linear as a result of stiffness deterioration corresponding to the deflection hardening period. The deterioration develops with the load increasing until the ultimate load is obtained. After that, there was a decrease in load until the fracture point, often named the deflection softening period. The deflection softening period seems to be more important, accompanying a larger deflection value for high replacing content of crushed oyster shell cases. This explains why more ductile failure modes appeared in G3 specimens. Also, the addition of textile layers was the most effective for G3 in terms of improving bearing capacity and stiffness. The ductility index (μ) of the specimens represents the ability of structural elements to endure inelastic deformation while maintaining their load-carrying capacity before failure. It is evaluated by the ratio of the mid-span deflection at ultimate load (Δu) to the mid-span deflection at the yield limit (Δy) (refer to Maras *et al.* [14]). The increase of the ductility index values depicted in Table 6 indicates that the addition of TRC layers enhances the structural ductility:

$$\mu = \frac{\Delta u}{\Delta y}. \tag{24}$$

The load–deflection responses show that the control beam TCB-R exhibits the highest stiffness and load capacity, peaking at over 217 kN with a deflection of around 2.5 mm. The beams with 20 and 40% COS replacements show reduced stiffness and load capacity, with the 20% COS beam reaching about 186 kN and the 40% COS beam just over 168 kN. The overall strength of the concrete decrease refers to the intrusion of COS, with higher COS content leading to greater reduction. The control beam TCB-R exhibits the highest stiffness, followed by the 20OSB-R beam and the 40OSB-R beam. This trend indicates that increasing the percentage of COSs reduces the stiffness of the beam. However, the 40% COS beams display enhanced ductility, as reflected in their more gradual decline in load capacity after reaching a peak load, compared to the sudden drop seen in the control beam.

The load–deflection curves in Figure 17 compare the performance of beams with 20% COS content, including an unstrengthened beam and two other reinforced beams, respectively, with two and three layers of TRC. The unstrengthened beam has the lowest load capacity,

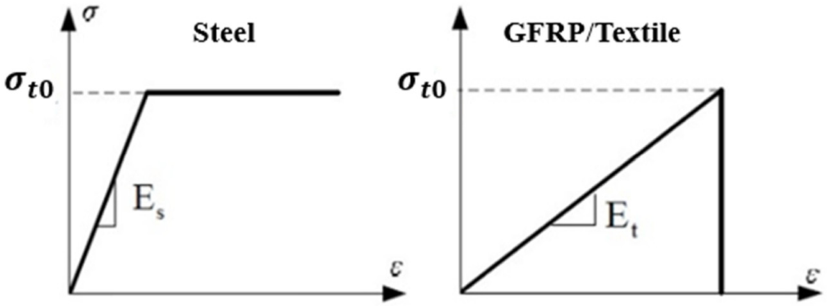

Figure 14: Stress–strain responses of steel and reinforcement (GFRP/textile).

peaking at around 186 kN with a deflection of 1.9 mm, indicating limited stiffness and strength. The beam reinforced with two TRC layers shows significant improvement, reaching approximately 266 kN at a 3 mm deflection, with much higher initial stiffness and sustained load capacity over a greater deflection range. The addition of TRC layers greatly enhances the structural performance of the beams, with three layers offering the most substantial improvement, which is around 283 kN of ultimate load at a deflection of 2.9 mm. The strengthened beams exhibit significantly higher load capacity and stiffness, demonstrating the reduced strength caused by the partial replacement of aggregates with COS was compensated by the effectiveness of the TRC layer.

The load–deflection curves in Figure 18 illustrate the performance differences among beams with 40% COS content, comparing the two beams strengthened with either two or three layers of carbon textile to one unstrengthened beam. The unstrengthened beam 40OSB-R reaches a peak load of approximately 168 kN with a deflection of around 2.2 mm, showing the lowest stiffness and strength among the three, as indicated by its gradual load increase with deflection. In contrast, the beam reinforced with two carbon layers exhibits a much steeper curve, indicating improved stiffness and reaching a peak load of about 235 kN, corresponding to a deflection of 2.5 mm. The three-layer TRC beam performs the best, peaking at around 267 kN at a deflection of 2.3 mm, demonstrating superior stiffness and load-bearing capacity. The TRC reinforcement clearly enhances the structural integrity of the beams, with the three-layer TRC beam offering the highest performance. Even the two-layer TRC beam shows significant improvement over the unstrengthened beam, underscoring the effectiveness of TRC in compensating for the reduced strength associated with high COS content.

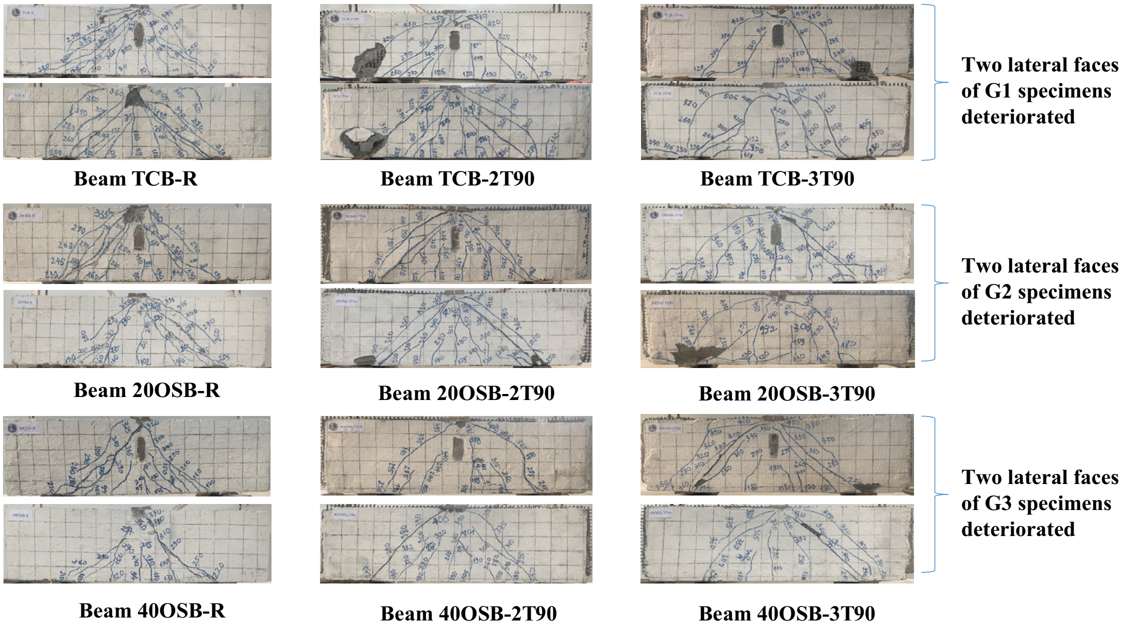

Figure 15: Crack patterns of all test beams.

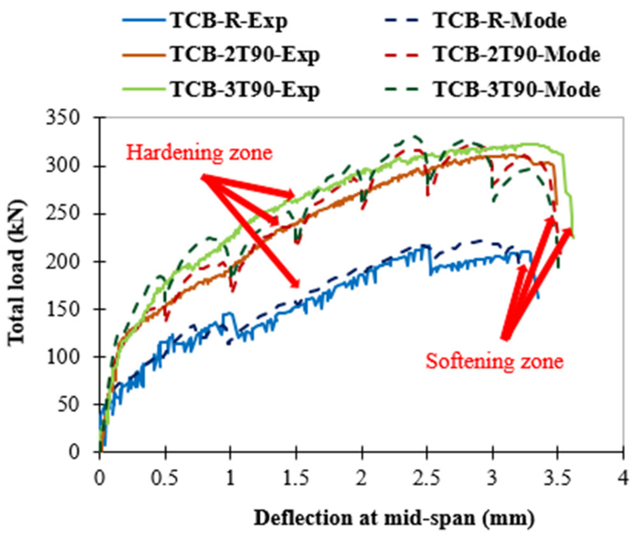

Figure 16: Load *vs* deflection of the three beams in the G1 group.

The overall shear capacity of beams includes a part of the GFRP rebar, the other part of concrete, and the contribution of the TRC material. Using shear prediction from four specifications such as JSCE 1997, CSA S806-12, ACI 440.1R-15, and BS-8110 [61–64], Tu *et al.* [65] found that compared to conventional concrete, OSC provides a lower nominal shear resistance. These predicted results are lower than the shear provision obtained from experiments on RC beams with GFRP rebar, ranging from 28 to 49%. As shown in Table 6, ACI 440.1R was selected for the shear provision of both reinforcement and concrete. Otherwise, the application of TRC in the shear strengthening of RC structures has been extensively studied over the past decade. However, no design codes currently exist for such structures (refer to Tran *et al.* [31]). The shear strength of the TRC layer can be calculated using the guidelines for FRP strengthening layers, as defined in ACI 440.2R [66].

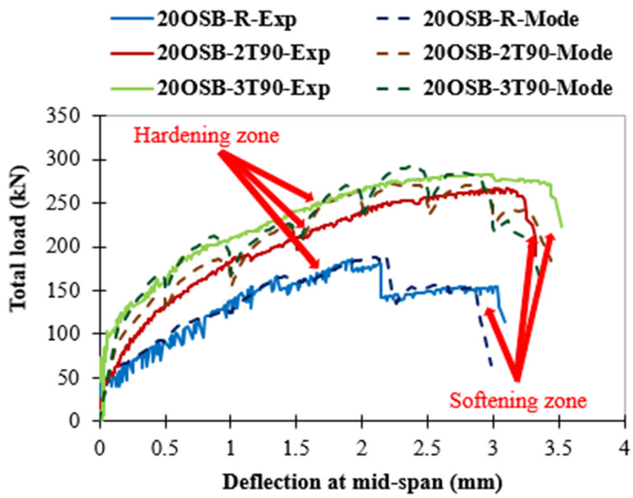

Figure 17: Load *vs* deflection of the three beams in the G2 group.

The specimens strengthened with two layers of carbon textiles showed a significant amelioration in the shear capacity and deflection. The shear capacity of the 0% oyster shell beam increased by approximately 44% (from 108 to 156 kN), while the 20 and 40% oyster shell beams saw improvements of 43% (from 93 to 134 kN) and 39% (from 84 to 118 kN). The addition of a third TRC layer resulted in the highest observed shear capacities. The shear capacity of the 0% oyster shell beam increased by 49% (from 108 to 162 kN), while those with 20 and 40% OSC showed improvements of 52% (from 93 to 142 kN) and 58% (from 84 to 134 kN). An adjustment of the COS content clearly ameliorated the ductility index of specimens, interpreted by a more dominant deflection softening zone on G3 specimens against load–deflection responses.

These findings seem to be in good agreement with the experimental results by Tran *et al.* [31], where an improvement in shear resistance by TRC strengthening was

Table 6: Theoretical and experimental comparison of the ductility index and shear behavior of all test beams

Specimen	Yield load Pcr (kN)	Δ*y* (mm)	Ultimate load Pu (kN)	Δ*u* (mm)	Ductility index *μ* (Δ*u*/Δ*y*)	Pcr/Pu	Shear strength by ACI440.1R/ACI 440.2R (kN)	Shear strength by experiment (kN)
TCB-R	81.01	0.27	216.61	2.52	9.3	37%	47.07	108.31
TCB-2T90	130.12	0.28	310.94	3.16	11.3	42%	71.22	155.47
TCB-3T90	168.23	0.34	323.24	3.42	10.1	52%	79.43	161.62
20OSB-R	71.89	0.28	186.29	1.92	6.9	39%	45.25	93.15
20OSB-2T90	84.99	0.23	266.21	3.11	13.5	32%	69.40	133.11
20OSB-3T90	113.71	0.26	283.43	2.93	11.3	40%	77.61	141.72
40OSB-R	69.47	0.37	168.16	2.15	5.8	41%	44.52	84.08
40OSB-2T90	76.98	0.25	235.08	2.45	9.8	33%	68.67	117.54
40OSB-3T90	119.78	0.28	266.96	2.29	8.2	45%	76.88	133.48

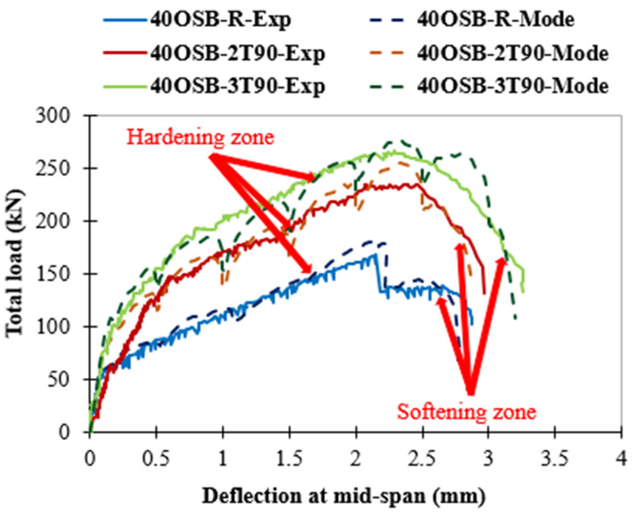

Figure 18: Load *vs* deflection of the three beams in the G3 group.

observed, ranging from 36.2 to 66.4% (*a*/*d* = 2.3) and from 33.9 to 83.1% (*a*/*d* = 2.8) with one and two layers of textile, respectively. The peaks of load–deflection relationship allows the prediction of the shear strength of beams depending on the replacing ratio of oyster shell and other mechanical properties with different strengthening methods, as presented in Figures 19–22.

The partial replacement of COSs for natural sand in the concrete mix had a noticeable impact on both stiffness and shear capacity. As the percentage of COSs increased, the initial stiffness decreased across all beam groups. This reduction in stiffness was reflected in the load–deflection curves in the initial portion, which became less steep with higher OSC, indicating a diminution in the elastic modulus of the concrete. Despite this diminution, the application of TRC significantly mitigated the adverse effects. Figure 23 displays the stress distribution of the GFRP rebar at the

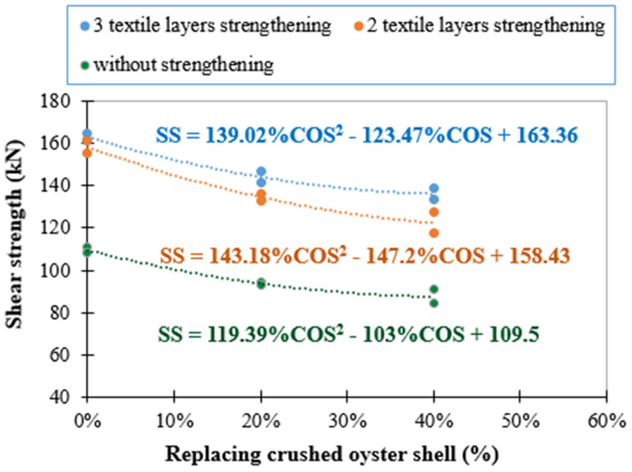

Figure 19: Shear strength *vs* replacing COS (in %).

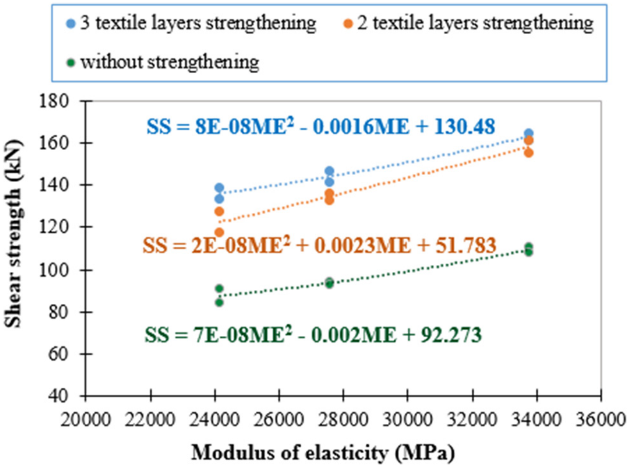

Figure 20: Shear strength *vs* modulus of elasticity corresponding to different COS contents.

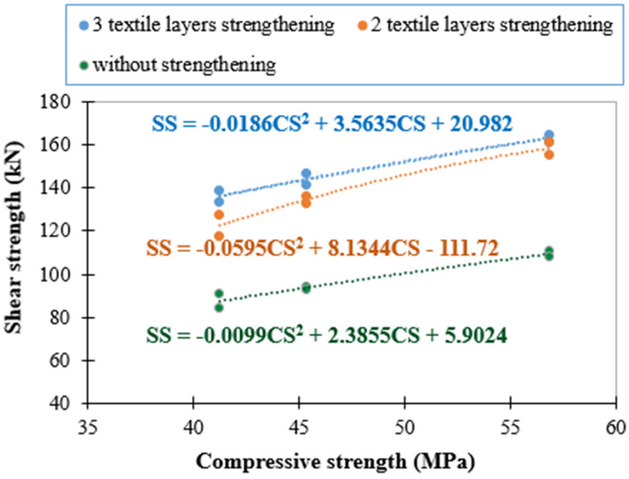

Figure 21: Shear strength *vs* compressive strength corresponding to different COS contents.

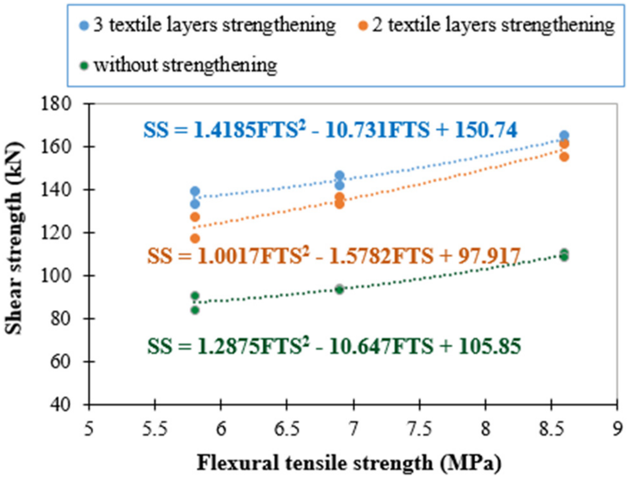

Figure 22: Shear strength *vs* flexural tensile strength corresponding to different COS contents.

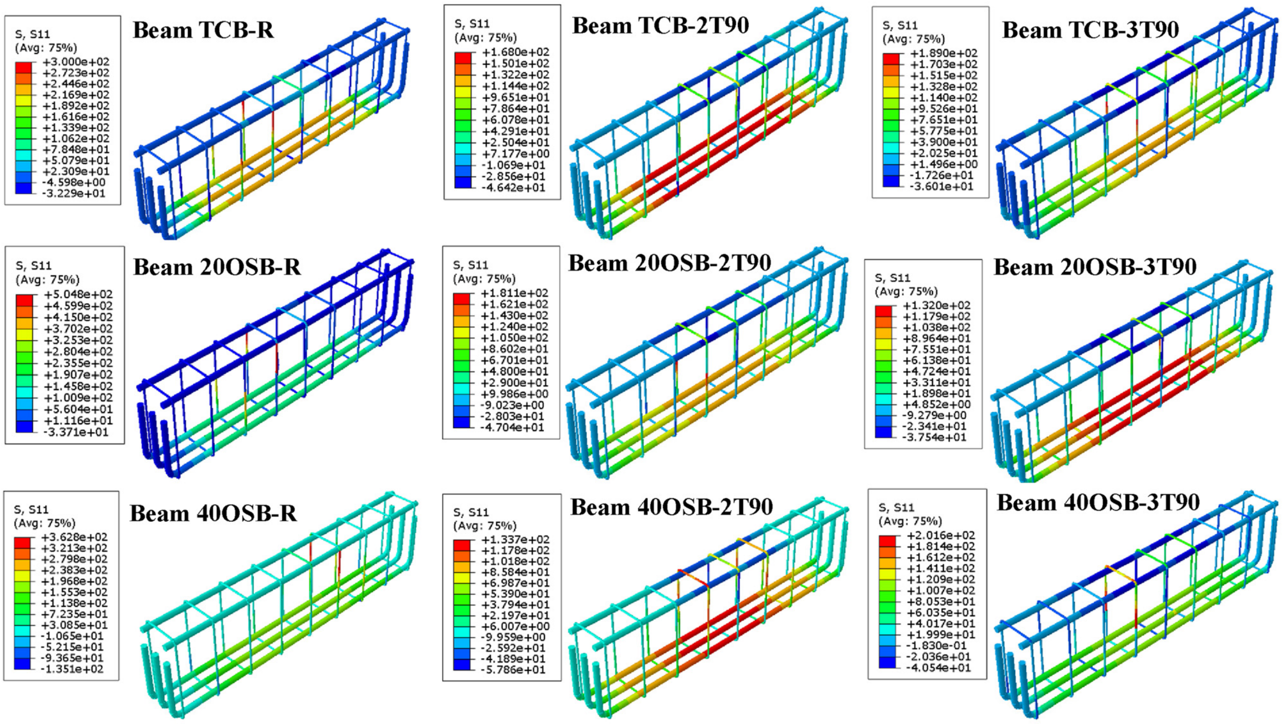

Figure 23: Stress distribution on the GFRP rebar at ultimate states of nine study cases.

Table 7: Maximal stress of rebar at ultimate states corresponding to different beam specimens

	Maximal stress by modeling (MPa)			Maximal stress by measurement (MPa)		
Specimen	**Top**	**Bottom**	**Stirrup**	**Bottom (SG3)**	**Stirrup (SG1)**	**Stirrup (SG2)**
TCB-R	−32.2	244.6	300.0	268.8	333.3	321.8
TCB-2T90	−46.4	168.0	150.1	198.3	310.2	307.5
TCB-3T90	−36.0	151.5	189.0	180.9	280.6	283.3
20OSB-R	−33.7	190.7	504.8	212.2	298.7	301.2
20OSB-2T90	−47.0	143.0	181.1	170.9	271.3	275.9
20OSB-3T90	−37.5	132.0	132.0	166.3	269.8	277.4
40OSB-R	−10.6	155.3	362.8	174.3	295.9	293.6
40OSB-2T90	−57.8	133.7	133.7	162.9	286.1	279.4
40OSB-3T90	−40.5	120.9	201.6	151.1	265.6	261.5

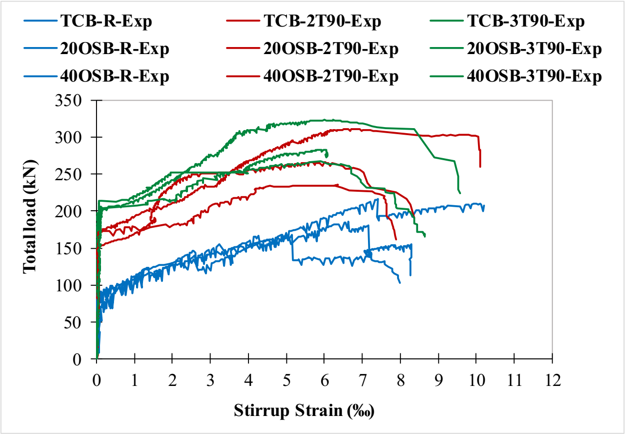

Figure 24: Load–strain relationships of GFRP stirrup in nine study cases.

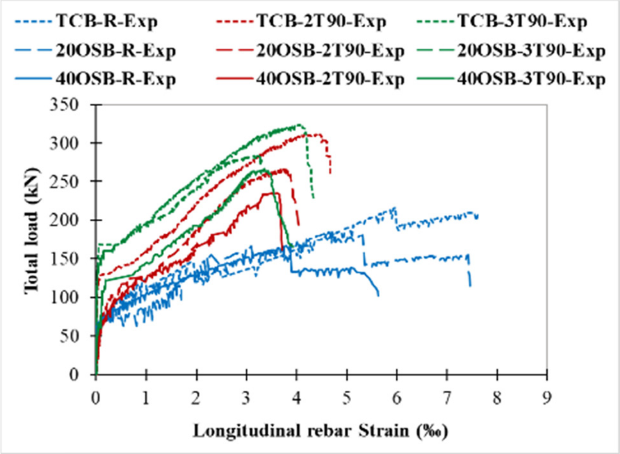

Figure 25: Load–strain relationships of GFRP longitudinal rebar in nine study cases.

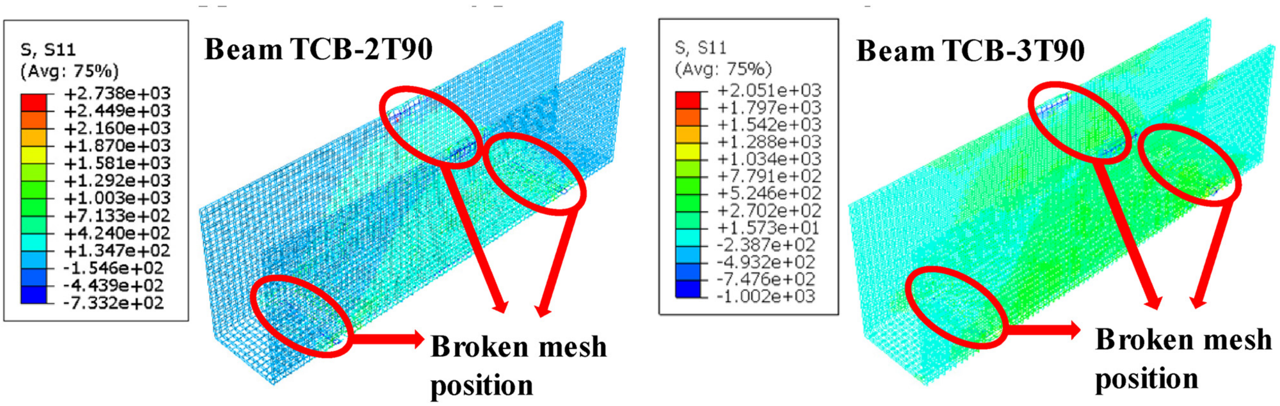

Figure 26: Stress distribution on the textile in the cases of strengthening by two and three textile layers.

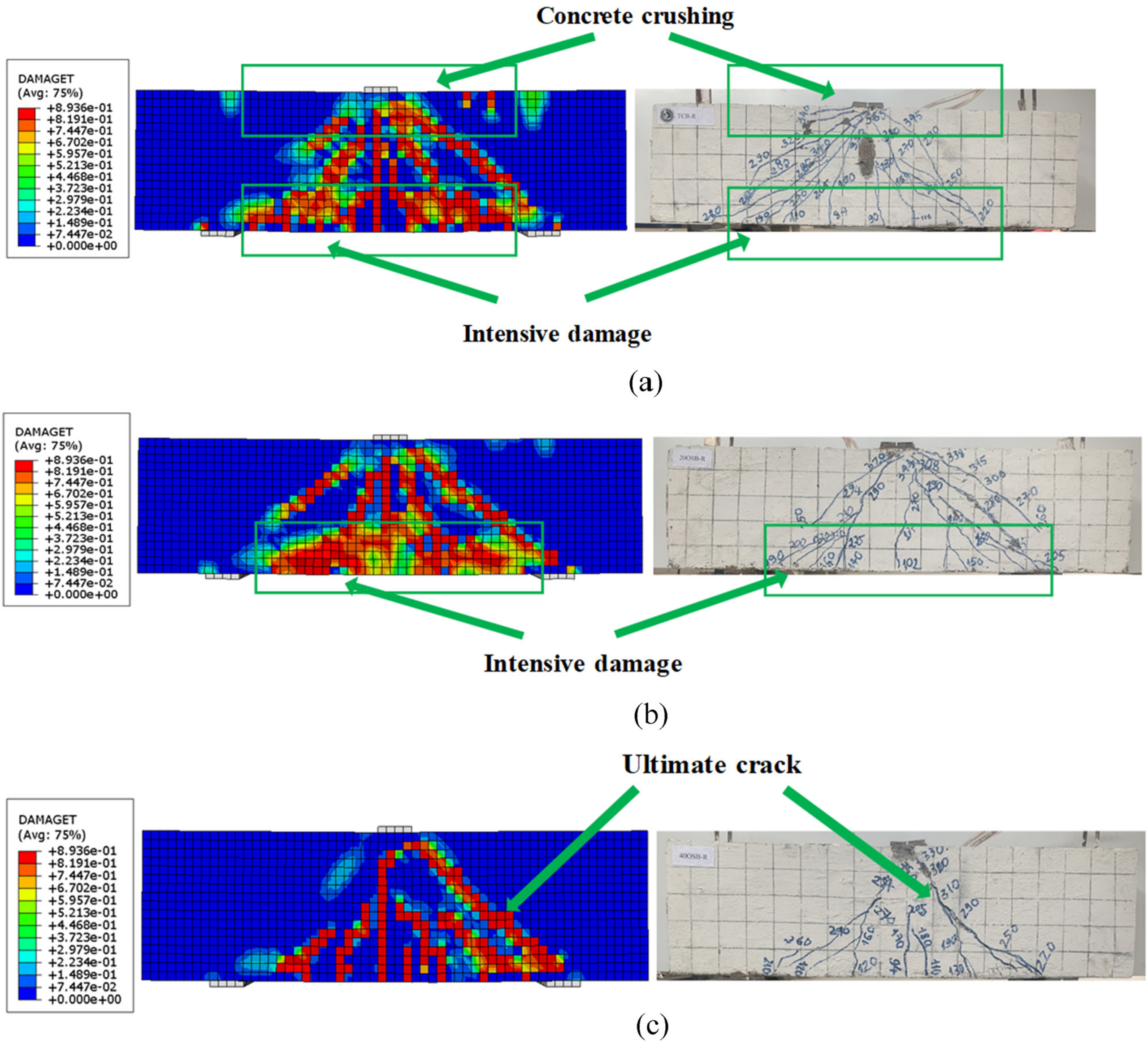

Figure 27: Comparison of failure pattern given by modeling and experiment of beams without strengthening. (a) Beam TCB-R. (b) Beam 20OSB-R. (c) Beam 40OSB-R.

ultimate states of all beams tested, which gives the maximal stress values compared to the results obtained by the experiment, as presented in Table 7. Due to the hypothesis of the ideal bond between the different materials, the experimental values of maximal stress on the GFRP rebar slightly exceeded those of the modeling. This means that the bearing capacity of both the master beam and TRC are overestimated numerically.

In general, textile layers proved their efficiency in strengthening, above all, toward three textile layers. Specifically, the maximal stress at ultimate states reveals significant differences in performance based on the level of TRC reinforcement, reflected by a more modest stress distribution on the GFRP rebar. The load–strain curves displayed in Figures 24 and 25 illustrate the effect of TRC strengthening on both stirrup and bottom reinforcement. At the same applied load, lower strain values were observed in the strengthened beams. The overall strain of the longitudinal rebar is significantly lower in the case of TRC-strengthened specimens.

Considering the bottom reinforcement and stirrup, the un-strengthened beams indicate early and significant stress, reflecting lower stiffness and load distribution capacity. Otherwise, the beams with two TRC layers show improved load capacity, with reinforcement stress remaining more controlled. The three-layer TRC beam performs the best, reaching a gradual increase in stirrup stress, demonstrating superior stiffness and better load management. TRC reinforcement clearly enhances both load capacity and stress control, with three layers providing the most effective improvement.

The numerical results in stress distribution proved that during the test, the fracture of GFRP rebar did not occur; meanwhile, several positions in the textile around the two supports and loading point were broken, as shown in Figure 26.

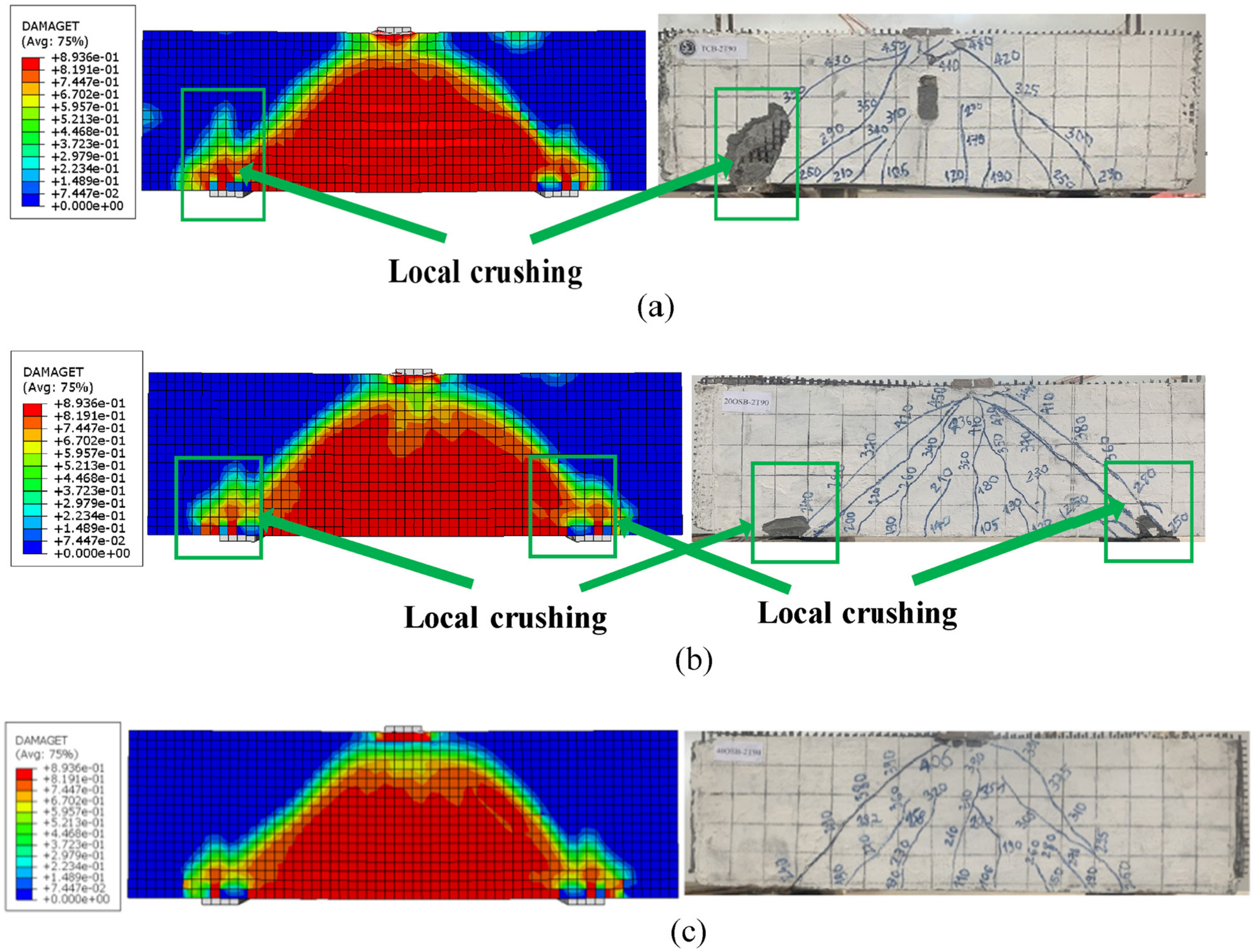

Figure 28: Comparison of failure pattern given by modeling and experiment of beams strengthened by two textiles layers. (a) Beam TCB-2T90. (b) Beam 20OSB-2T90. (c) Beam 40OSB-2T90.

4.2 Influence of crushed OSC on shear performance of beams without strengthening

Indeed, different failure modes could be identified through structural responses. The efficacy and reliability of the proposed model were verified by comparing it with test results corresponding to each case, as shown in Figure 27. As previously discussed, the control beam TCB-R demonstrated the shear failure method owing to the transmission of fine shear cracks inside the shear zone across the diagonal direction, connecting two supports and the loading point with the crushing of concrete in the compression zone. During the loading process, the fine cracks were extended and propagated intensively in the tensile zone.

Against beam 20OSB-R, intensive cracks were identically notified in the tension zone, but concrete crushing was not observed. It seems that the COS content increase reduced the shear performance. Consequently, the failure pattern is less brittle in the ultimate state. In the case of 40% COS content, due to a weaker ultimate load, the shear cracks appeared sparsely, with a diagonal crack connecting the loading point and one of the supporting pins at the end of the test. This observation was confirmed by both numerical and experimental results.

4.3 Influence of TRC thickness strengthening on shear behavior of strengthened beams

As mentioned above, under strengthening by multiple TRC layers, several properties of beams were ameliorated, such as the stiffness or shear performance, leading to a different failure pattern. Figures 28 and 29 compare the experimental and numerical failure patterns, respectively, in the case of two and three textile layer strengthening. A parabolic damage zone of fine grain concrete relying loading point and two supports at two lateral faces of specimens was alerted in strengthened beams with two textile layers. Likewise, the damage zone is more inflated for the strengthened beams with three textile layers, corresponding to a higher collapse level of specimens. In several

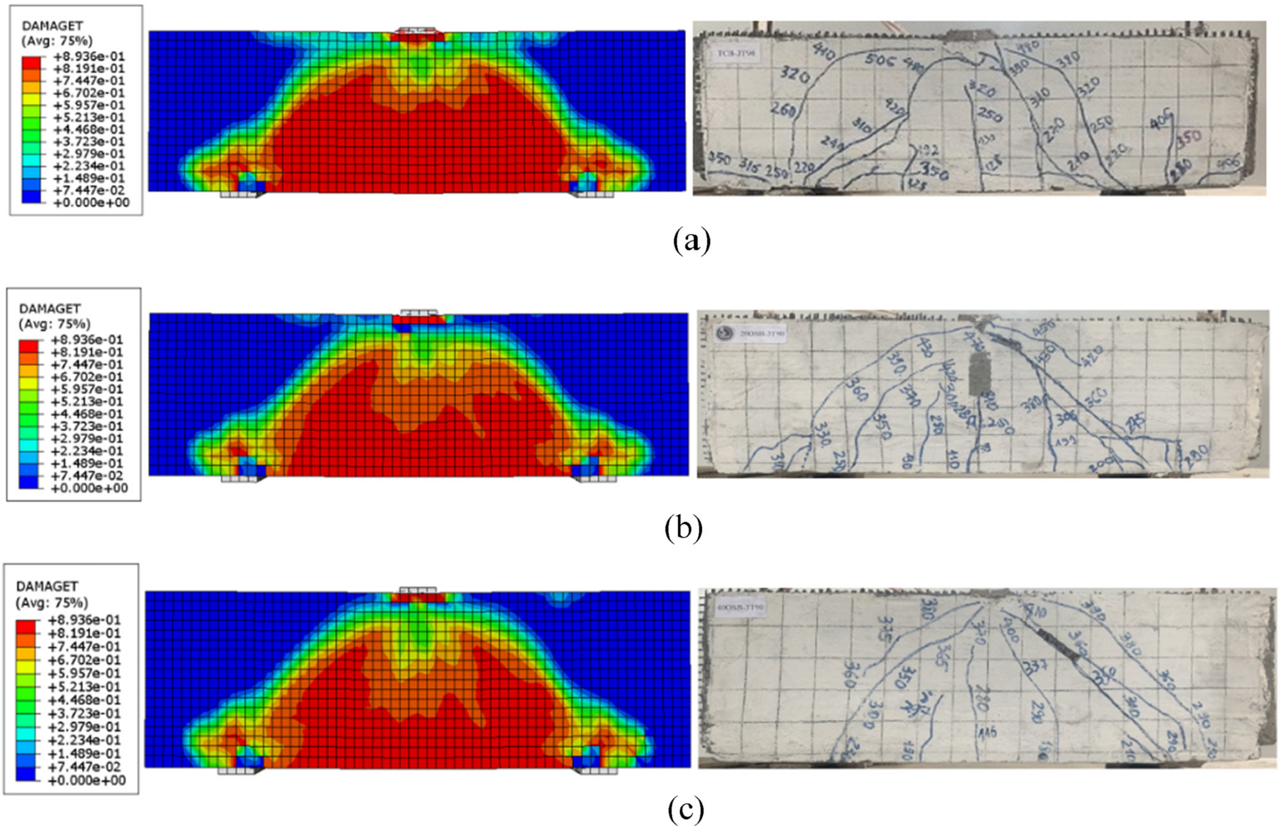

(a)

(b)

(c)

Figure 29: Comparison of failure pattern given by modeling and experiment of beams strengthened by three textiles layers. (a) Beam TCB-3T90. (b) Beam 20OSB-3T90. (c) Beam 40OSB-3T90.

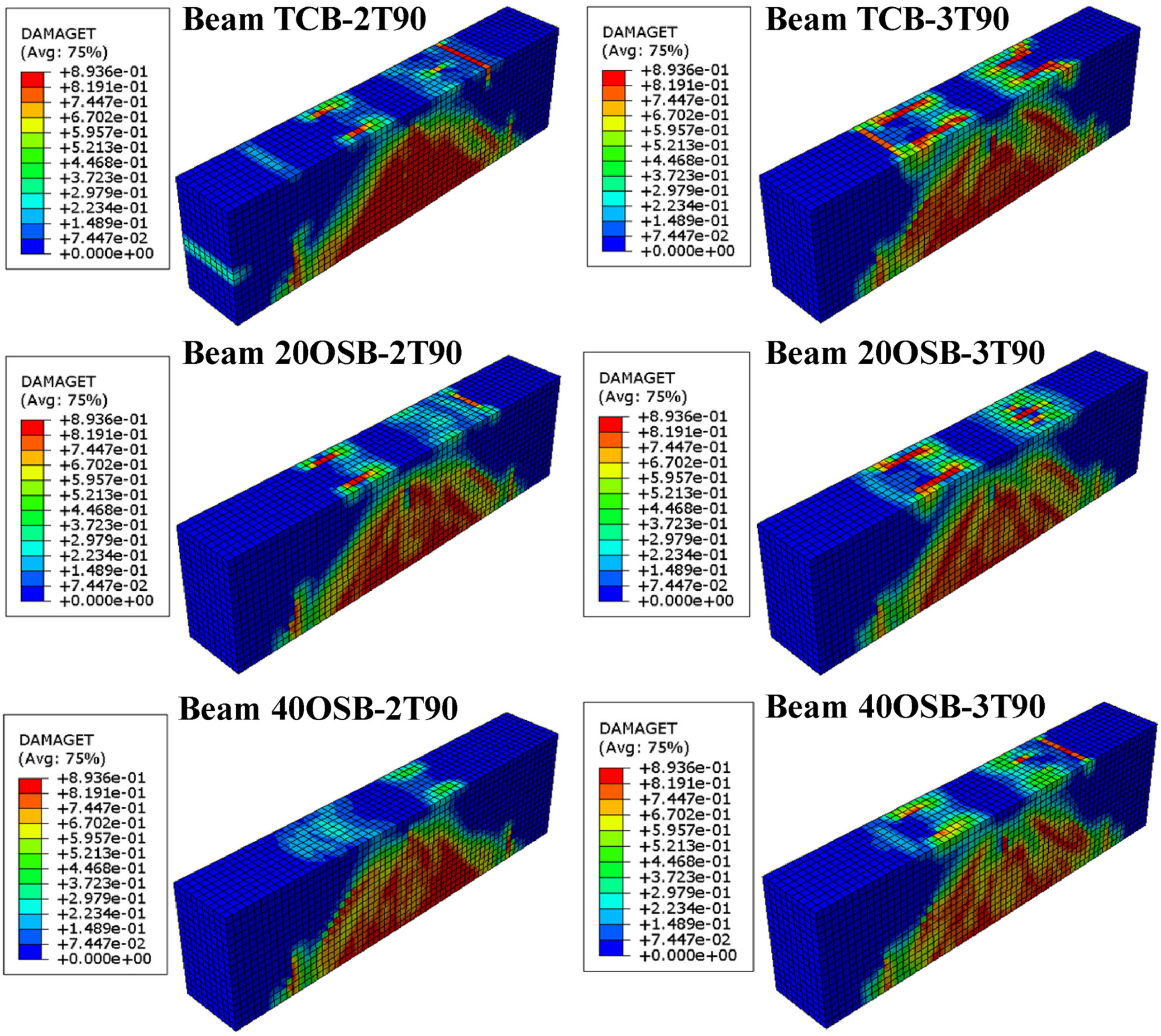

Figure 30: Failure pattern, given by modeling of six master beams strengthened by TRC.

specimens belonging to G1 or G2, for example, there exists many local crushing of concrete around two supports. This occurrence justified that there is a very good match between the experiment and modeling. Besides, neither concrete crushing is noted for G3 specimens, proving an amelioration in the ductility of materials.

Furthermore, Figure 30 assesses numerically the collapse method of all master beams strengthened by TRC. This analysis brought a vision that was unavailable to be achieved by experimental observation. At the same replacing ratio of COS, the addition of textile layers enhances the stiffness and the ultimate load, yielding more apparition of concrete crushing in the compression zone and less flexural cracks in the tension zone. Indeed, more diagonal cracks were observed due to shear failure at the two lateral faces of specimens. On the other hand, at the same level of textile layer strengthening, as the ultimate loads and stiffness decline with the adjustment of COS, the damage level of specimens considered also seems vaguer as well.

5 Conclusions

Despite the reduction in shear behavior, the combination of OSC with GFRP rebar, especially in strengthening TRC, could be a promising solution for the manufacturing of precast components under shear solicitation. The following conclusions were drawn based on the analysis results.

It is necessary to highlight that with the COS replacement as fine aggregate, several mechanical properties such as compressive strength, modulus of elasticity, and flexural tensile strength of OSC decreased compared to those of traditional concrete with a specified compressive strength of 56.8 MPa. This was maybe related to the main mineral components of the oyster shell, the $CaCO_3$ group, which has a much lower hardness than those of natural sand, the SiO_2 group. Additionally, the irregular form of COS grains contributes to the heterogeneity of material, leading to a resonant effect. The analysis results at the microscale also confirmed the above statement. Moreover, a constitutive numerical model was created as a way to better understand the effect of OS content and quantity of TRC layers on the shear behavior. To ensure the reliability of the proposed model, many three-point bending tests on short-span beams were performed. The shear capacity of each beam was calculated based on the maximum load recorded during the testing process. A clear trend emerged, showing that TRC significantly upgraded the shear strength of the considered beams, with the extent of improvement dependent on the number of TRC layers and the crushed oyster shell percentage in the concrete mix. The control beams with 0, 20, and 40% crushed OSC exhibited the lowest shear capacities, ranging experimentally from 108 to 84 kN. The increasing OSC correlated with a reduction in stiffness, shear capacity and also deflection, highlighting the limitations of this alternative aggregate in resisting shear forces.

On the whole, the numerical model not only successfully reproduced the failure pattern and load–deflection relationship of all specimens tested but also gave a valuable explication of the overall behavior of the structure, the predictions of shear strength depending on the COS content, and also on other mechanical properties. These results underscore the effectiveness of multiple TRC layers in significantly enhancing the shear strength of RC beams, even when using non-traditional aggregate materials.

Funding information: This research is funded by the University of Transport and Communications (UTC) under grant number T2023-XD-002TD.

Author contributions: All authors have accepted responsibility for the entire content of this manuscript and approved its submission.

Conflict of interest: Authors state no conflict of interest.

Data availability statement: The datasets generated during and/or analyzed during the current study are available from the corresponding author on reasonable request.

References

[1] Sickels-Taves LB, Sheehan MS. The lost art of tabby redefined: Preserving oglethorpe's architectural legacy. Southfield, MI: Architectural Conservation Press; 1999.
[2] Morris SD. Tabby. New Georgia. Encyclopedia, last modified Sep 10, 2019. https://www.georgiaencyclopedia.org/articles/historyarchaeology/tabby.
[3] Steven DP, Dieter BB, Kunal K-P, Admir M, Markus JB, Oral B. Roadmap across the mesoscale for durable and sustainable cement paste – A bioinspired approach. Constr Build Mater. 2016;115:13–31.
[4] Monita O, Annisa AM, Lita D. Mechanical properties of seashell concrete. Procedia Eng. 2015;125:760–4.
[5] Uchechi GE, John CE, Bennett IE. Properties of seashell aggregate concrete: A review. Constr Build Mater. 2018;192:287–300.
[6] Zhiquan X, Yi G, Yao Z, Libo Ch, Kwok-Fai Ch, Yu Ch. Deterioration pattern of the axial compressive properties of steel-reinforced concrete columns owing to chloride salt erosion. Eng Struct. 2024;313:118169.
[7] Won J-P, Park C-G, Lee S-J, Hong B-T. Durability of hybrid FRP reinforcing bars in concrete structures exposed to marine environments. Int J Struct Eng. 2013;4(1–2):63–74.
[8] Micelli F, Nanni A. Durability of FRP rods for concrete structures. Constr Build Mater. 2004;18(7):491–503.
[9] Hegger J, Will N, Rüberg K. Textile reinforced concrete – A new composite material. Advances in construction materials 2007. Grosse CU, editor. Berlin. Heidelberg: Springer Berlin Heidelberg; 2007. p. 147–56.
[10] Brameshuber W. Textile reinforced concrete - state-of-the-art report of RILEM TC 201-TRC, Proceedings of the International RILEM. ed; 2006. p. 292.
[11] Chinyere ON, Mahachi J, Olukanni DO, Musonda I. Natural fibres and biopolymers in FRP composites for strengthening concrete structures: A mixed review. Constr Build Mater. 2023;363:129661.
[12] Maras MM, Yurtseven HB, Ozdemir MF. Failure analysis of laminated wooden arches strengthened with novel carbon-fiber-reinforced polymer (CFRP) composites: An experimental study. J Korean Wood Sci Technol. 2024;52(6):585–604.
[13] Kantarci M, Maras MM, Ayaz Y. Experimental performance of RC beams strengthened with aluminum honeycomb sandwich composites and CFRP U-jackets. Exp Tech. 2023;47(4):767.
[14] Maras MM, Kantarci F. Structural performance of reinforced concrete (RC) moment frame connections strengthened using FRP composite jackets. Arab J Sci Eng. 2021;46:10975–92.
[15] Ali MI, Allawi AA, El-Zohairy A. Flexural behavior of pultruded GFRP–concrete composite beams strengthened with GFRP stiffeners. Fibers. 2024;12:7.
[16] Issa MA, Allawi AA, Oukaili N. Effects of GFRP stirrup spacing on the behavior of doubly GFRP-reinforced concrete beams. Civ Eng J. Feb. 2024;10(2):502–20.

[17] Issa MA, Allawi AA, Oukaili N. Performance of doubly reinforced concrete beams with GFRP bars. J Mech Behav Mater. 2024;33:20220308.

[18] Mahmood EM, Allawi AA, El-Zohairy A. Flexural performance of encased pultruded GFRP I-beam with high strength concrete under static loading. Materials. 2022;15:4519.

[19] Mahmood EM, Ibrahim TH, Allawi AA, El-Zohairy A. Experimental and numerical behavior of encased pultruded GFRP beams under elevated and ambient temperatures. Fire. 2023;6:212.

[20] Xing Z, Zhu Y, Shao Y, Ma E, Chung K-F, Chen Y. Experimental and numerical research on shear performance of GFRP bar reinforced seawater sea-sand concrete deep beams without stirrups. Case Stud Constr Mater. 2024;20:e03142.

[21] Benny B, Bazli M, Rajabipour A, Arashpour M. Durability of tubular sea water sea sand concrete and fibre-reinforced polymer hybrid structures: Mechanisms and effective parameters: Critical overview and discussion. Constr Build Mater. 2023;366:130206.

[22] Zhang Q, Xiao J, Liao Q, Duan Z. Structural behavior of seawater sea-sand concrete shear wall reinforced with GFRP bars. Eng Struct. 2019;189:458–70.

[23] Maras MM, Kantarci F. Structural behavior of RC beams strengthened using fiber-reinforced polymer U-jackets. Struct Concr. 2023;24(2):2384–401.

[24] Nguyen TT, Selvaraj S, Chan T-M, Mottram JT. Influence of combined imperfections on lateral-torsional buckling behaviour of pultruded FRP beams. Composite Struct. 2023;304:116385.

[25] Maras MM. Mechanical properties of confined damaged concrete strengthened with fibre reinforced polymer wraps. El-Cezerî J Sci Eng. 2021;8(2):706–17.

[26] Azam R, Soudki K, Jeffrey SW, Noël M. Shear strengthening of RC deep beams with cement-based composites. Eng Struct. 2018;172:929–37.

[27] Tran TT, Tu SQ. Experimental and numerical investigation on bearing behavior of TRC slabs under distributed or concentrated loads. Adv Intell Syst Comput. 2021;1284:504–16.

[28] Peled A, Sueki S, Mobasher B. Bonding in fabric-cement systems: Effects of fabrication methods. Cem Concr Res. 2006;36:1661–71.

[29] Peled A, Zaguri E, Marom G. Bonding characteristics of multifilament polymer yarns and cement matrices. Compos: Part A. 2008;39:930–9.

[30] Si Larbi A, Contamine R, Ferrier E, Hamelin P. Shear strengthening of RC beams with textile reinforced concrete (TRC) plate. Constr Build Mater. 2010;24(10):1928–36.

[31] Tran CTN, Nguyen XH, Nguyen HC, Le DD. Shear performance of short-span FRP-reinforced concrete beams strengthened with CFRP and TRC. Eng Struct. 2021;242:112548.

[32] Rossi E, Randl N, Harsányi P, Mészöly T. Experimental study of fiber-reinforced TRC shear strengthening applications on non-stirrup reinforced concrete T-beams. Eng Struct. 2022;256:113923.

[33] Tran CTN, Nguyen XH, Nguyen NB, Pham MH. Shear behaviour of GFRP reinforced concrete beams strengthened by textile reinforced concrete. Transp Commun Sci J. 10/2021;72(8):932–44.

[34] Bui TTM, Nguyen HC, Ngo DQ, Dinh HT. Experimental study on flexural and shear behaviour of sandwich panels using glass textile reinforced concrete and autoclaved aerated concrete. Transp Commun Sci J. 1/2020;71(1):18–26.

[35] ASTM C33 -18. Standard specification for concrete aggregates; 2018.

[36] ACI 211.4R-08. Guide for selecting proportions for high-strength concrete using portland cement and other cementitious materials; 2008.

[37] ASTM D7205M-21. Standard test method for tensile properties of fiber reinforced polymer matrix composite bars; 2021.

[38] ASTM C348-21. Standard test method for flexural strength of hydraulic-cement mortars; 2021.

[39] ASTM C349-18. Standard test method for compressive strength of hydraulic-cement mortars (using portions of prisms broken in flexure); 2018.

[40] ACI 549.4R-20. Guide to design and construction of externally bonded fabric-reinforced cementitious matrix and steel-reinforced grout systems for repair and strengthening of concrete structures; 2020.

[41] ASTM C39 / C39M - 17b. Standard test method for compressive strength of cylindrical concrete specimens; 2017.

[42] ASTM C469–02. Standard test method for static modulus of elasticity and poisson's ratio of concrete in compression; 2002.

[43] ASTM C78 – 02. Standard test method for flexural strength of concrete (using simple beam with third-point loading); 2002.

[44] SIMULIA. Analysis user's manual version 6.14. Dassault Systemes Simulia, Inc., USA; 2014.

[45] Vervloet J, Tysmans T, Kadi M, Matthias D-M. Validation of a numerical bending model for sandwich beams with textile-reinforced cement faces by means of digital image correlation. Appl Sci. 2019;9(6):1253.

[46] Hognestad E. A study of combined bending axial load in reinforced concrete members Bulletin Series No 399, vol 49 Engineering Experimental Station. Urbana: The University of Illinois; 1951.

[47] Nguyen GD, Korsunsky AM. Development of an approach to constitutive modelling of concrete: isotropic damage coupled with plasticity. Int J Solids Struct. 2008;45:5483–501.

[48] Lubliner J, Oliver J, Oller S, Onate E. A plastic-damage model for concrete. Int J Solids Struct. 1989;25(3):299–326.

[49] Lee J, Fenves GL. Plastic-damage model for cyclic loading of concrete structures. J Eng Mech. 1998;124(8):892–900.

[50] Ayhan B, Lale E. Modeling strain rate effect on tensile strength of concrete using damage plasticity model. Int J Impact Eng. 2022;162:104132.

[51] Kazemi M, Madandoust R, Chastre C, Esfahani MR, Courard L. Numerical study on the flexural behaviour of normal- and high-strength concrete beams reinforced with GFRP bar, using different amounts of transverse reinforcement. Structures. 2021;34:3113–24.

[52] Tawfik AB, Mahfouz SY, Taher SE-DF. Nonlinear ABAQUS simulations for notched concrete beams. Materials. 2021;14:7349.

[53] Antoniou M, Nikitas N, Anastasopoulos I, Fuentes R. Scaling laws for shaking table testing of reinforced concrete tunnels accounting for post-cracking lining response. Tunn Undergr Space Technol. 2020;101:103353.

[54] ACI 224.2R-92. Cracking of concrete members in direct tension. Reapproved 1997.

[55] Zheng Y-Z, Wang W-W, Mosalam K-M, Fang Q, Chen L, Zhu Z-F. Experimental investigation and numerical analysis of RC beams shear strengthened with FRP/ECC composite layer. Compos Struct. 2020;246:112436.

[56] Madandoust R, Kazemi M, Moghadam SY. Analytical study on tensile strength of concrete. Romanian J Mater. 2017;47(2):204–9.

[57] Shawki Ali NK, Mahfouz SY, Amer NH. Flexural response of concrete beams reinforced with steel and fiber reinforced polymers. Buildings. 2023;13:374.

[58] Abdelwahed BS, Kaloop MR, El-Demerdash WE. Nonlinear numerical assessment of exterior beam-column connections with low-strength concrete. Buildings. 2021;11:562.
[59] Ahmed L. Dynamic measurements for determining poisson's ratio of young concrete. Nordic Concrete Research. 2018;58(1): 95–106.
[60] Pal P. Dynamic Poisson's ratio and modulus of elasticity of pozzolana Portland cement concrete. Int J Eng Technol Innov. 2019;9(2):131–44.
[61] JSCE 1997. Code FRP concrete structures using continuous fiber reinforcing; 1997.
[62] CSA S806-12. Design and construction of building structures with fibre-reinforced polymers; 2012.
[63] ACI 440.1R-15. Guide for the design and construction of structural concrete reinforced with fiber-reinforced polymer bars; 2015.
[64] BS 8110-1997. Structural use of concrete; 1997.
[65] Tu SQ. Influence of fine aggregates replaced ratio on shear strength of oyster shell concrete beam using GFRP rebars. Transp Commun Sci J. 09/2024;75(7):2139–53.
[66] ACI 440.2R-17. Guide for the design and construction of externally bonded FRP systems for strengthening concrete structures; 2017.